IEEE Open Journal of
Power Electronics

Received 3 April 2024; accepted 26 April 2024. Date of publication 30 April 2024;
date of current version 9 May 2024. The review of this article was arranged by Associate Editor Cong Li.

Digital Object Identifier 10.1109/OJPEL.2024.3395174

Comparative Analysis of Wireless Power Transfer Couplers for Unmanned Aerial Vehicles and Drones

UVIR GORDHAN (Student Member, IEEE) AND SAMPATH JAYALATH (Member, IEEE)

Department of Electrical Engineering, University of Cape Town, Cape Town 7700, South Africa

CORRESPONDING AUTHOR: SAMPATH JAYALATH (e-mail: sampath.jayalath@uct.ac.za)

This work was supported in part by the National Research Foundation of South Africa, in part by the University of Cape Town, and in part by the Department of Science and Innovation of South Africa.

ABSTRACT Several magnetic couplers have been presented for IPT-based charging of unmanned aerial vehicles (UAV) with different sizes, transmission distances, power ratings, and landing gears. Therefore, it is hard to conclude the superiority or suitability of existing couplers for a given UAV application without evaluating their performance under common indices. Thus, a comparative analysis of existing IPT couplers for UAVs is conducted in this article, considering electromagnetic and physical performance indices. This includes efficiency, leakage magnetic field, misalignment tolerance, receiver coil volumetric power density, weight, and total harmonic distortion (THD) of transmitter and receiver currents. The validity of the analysis is experimentally supported. This article identifies the following: relative advantages and disadvantages of existing couplers, the best couplers suited for different landing gears of UAVs in the rotary-wing category, the impact of compensation on UAV coupler performance, and the best overall performing couplers. Moreover, future directions are suggested based on the drawbacks identified through analysis.

INDEX TERMS Coil design, drones, electromagnetic coupling, inductive power transfer, magnetic couplers, unmanned aerial vehicles (UAV), wireless power transfer.

I. INTRODUCTION

Wireless charging is a well-known field of research and has become increasingly popular for Unmanned Aerial Vehicle (UAV) or drone applications. UAVs/drones are aircrafts that can be controlled remotely. They are categorized into fixed wings, rotary wings, airships, Fixed-wing Hybrid Vertical Take-Off and Landing (VTOL), and flapping wings [1]. They are used in various applications, such as surveillance, agriculture, aerial mapping, and courier services [2]. One major drawback with these vehicles is the low battery capacity and the need for frequent charging. Some applications demand longer battery life to enable long-distance operation [1]. Thus, wireless charging offers a smart solution to improve a drone's operational longevity, as it can be autonomously charged once its battery runs out. It will contribute to the autonomous operation of large-scale units in the near future.

Wireless charging solutions proposed for UAVs are based on inductive power transfer (IPT) and capacitive power transfer (CPT) technologies [3]. CPT utilizes an electric field as the power transfer medium, while IPT uses a magnetic field [3]. However, this article focuses on IPT-based couplers that are proposed for UAVs.

A typical IPT system has input and output side power electronics and the magnetic coupler, which consists of the primary (*Tx*) and secondary (*Rx*) coils. When designing a magnetic coupler for IPT-based charging of UAVs, its electromagnetic design parameters, such as coil-to-coil efficiency, leakage magnetic field and misalignment tolerance, and physical features, such as volumetric power density and receiver coil weight, should be considered. Maximizing power transfer efficiency from the *Tx*-coil to the *Rx*-coil is the primary goal in WPT applications. The magnetic field generated by the coupler and high current harmonics may cause electromagnetic interference (EMI) with electronic components in its proximity. Therefore, it is crucial to minimize leakage field and THD. Misalignment between the *Tx*-coil and *Rx*-coil contributes to an increase in leakage magnetic fields and can decrease the power transfer capability of a coupler due to poor coupling

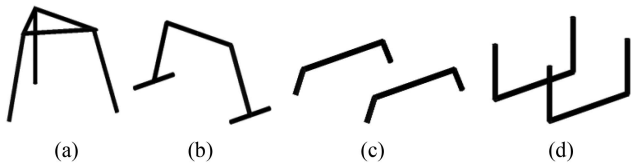

FIGURE 1. Rotary-wing UAV landing gears (a) tripod-shaped [8], (b) T-shaped, (c) short-legged [5], (d) U-shaped [9].

TABLE 1. Performance Indices

Variable	Criteria	Objective
η_c	Coil-to-Coil Efficiency	Max
$THD\%$	Total Harmonic Distortion	Min
α_V	Power Density	Max
d_{BLf}	Leakage Magnetic Field	Min
M_T	Misalignment Tolerance	Max
W_{Rx}	Weight of *Rx*-coil	Min

coefficient. Therefore, a high misalignment tolerance is desired. The drones are aerial vehicles, and keeping their weights as minimum as possible is desirable. Therefore, the weight of the *Rx*-coil should be kept at a minimum [1]. Lastly, the design and placement of the *Rx*-coil should consider the shape of the drone's landing gear. The category of UAVs most commonly used in applications is the rotary wing. These UAVs have different sizes and landing gears. Common landing gears for rotary-wing UAVs are illustrated in Fig. 1. The *Rx*-coil is typically designed to fit a specific landing gear and may have a different coil geometry to the *Tx*-coil. The *Tx*-coil is typically designed for optimal performance with the *Rx*-coil. Hence, the design of the *Rx*-coil in UAV applications is significantly important to ensure the geometric integrity of the UAV.

Several magnetic couplers using different coil geometries have been presented for IPT-based UAV charging [2], [4], [5], [6], [7], [8], [9], [10], [11], [12], [13], [14]. Planar non-polarized coils, such as circular [2], [4], [5], and square/rectangular coils [6], are common in UAV applications and couple with the perpendicular component of magnetic flux [15]. Planar polarized coils such as the double D (DD), Bipolar (BP), and double D-Quadrature (DDQ) coils can generate both parallel and perpendicular magnetic fields depending on current excitation. These are popular in electric vehicle (EV) applications but have been used as transmitters in UAV applications [9]. Non-planar coils couple with the parallel component of magnetic flux, are also presented for UAV applications. Based on the literature, these are typically variations of solenoid coils, such as non-planar circular [7], helical [8], rectangular [9], and trapezoidal [10].

A comparison of existing magnetic couplers for IPT-based UAV charging is absent in the literature. The size of the coils, ferrite utilization, transmission distance, operating frequencies, transferred power, and compensation methods differ between each design [2], [4], [5], [6], [7], [8], [9], [10], [11]. Furthermore, the design method and specification of certain design parameters are absent in some solutions. Therefore, it is difficult to conclude about the relative performance of these couplers. This article introduces a set of design parameters, and a design method is followed to compare existing couplers. Design parameters include electrical and physical constants such as required output power, maximum receiver coil size, conductor diameter, conductor spacing, and transmission distance. The design method involves identifying the battery specifications of a rotary-wing UAV and following the design parameters and constraints to realize each coupler. The contribution of this article compared to the existing literature is summarized as follows:

1. Identifies the advantages and disadvantages of existing couplers for UAVs based on key performance indices.
2. Identifies which coupler is suited for landing gears of UAVs currently used in commercial and industrial operations.
3. Identifies the impact of compensation choice on existing couplers in terms of transmission distance, operating frequency, and primary current.
4. Provides a thermal analysis of each coupler.
5. Provides an experimental analysis of a double-helix receiver for UAV WPT applications.

The rest of the article is structured as follows: Section II provides an overview of existing IPT couplers for UAVs. Section III contains a detailed discussion on the methodology. Simulation analyses aided by ANSYS Maxwell3D and MATLAB Simulink are provided in Section IV. The comparative analysis is validated with experimental results in Section V. A discussion of the results from the analysis is carried out in Section VI, and future directions are proposed in Section VII.

II. OVERVIEW OF UAV COUPLERS

Several wireless charging techniques for UAVs have been presented in the literature. Some autonomous charging applications have been found to use resonant magnetic coupling without a compensation method [13], [14]. Array configurations for the *Tx*-coil is also present [15], [16]. However, this article considers only single *Tx* and single *Rx*-coil couplers using compensation topologies. Magnetic couplers are typically designed to meet five common goals i.e., maximize coil-to-coil efficiency, maximize power density, minimize leakage magnetic field, maximize misalignment tolerance, and minimize receiver coil weight. This article includes an additional design goal of minimizing THD. These goals, illustrated in Table 1, are important to UAV applications and are therefore used as performance indices in this article.

The specifications of existing magnetic couplers considered in this study are illustrated in Table 2. IPT-based UAV chargers have been developed for small, medium, and large-sized UAVs with power levels ranging from 7–450 W. Based on

TABLE 2. Existing Magnetic Couplers

Coupler	*Rx*-coil Geometry	*Tx*-coil Geometry	Power (W)	Distance (mm)	Frequency (kHz)	Coupling (k_0)	Ferrite	Phase/Compensation
C1 [4]	Planar Circular	Planar Circular	70	100	150	0.14	No	1Φ/SP
C2 [2]	Planar Circular	Planar Circular	195	200	50	0.2	Yes	1Φ /SS
C3 [5]	Planar Circular	Planar Square	183.7	50	300	0.1	No	1Φ /LCC
C4 [6]	Planar Square	Planar Square	7	150	370	-	No	1Φ /SS
C5 [7]	Circular Solenoid	Planar Circular	10	100	1000	0.37	No	1Φ /SS
C6 [8]	Helical Solenoid	Helical Solenoid	150	2	60	0.45	Yes	3Φ /SS
C7 [9]	Rect. Solenoid	Planar DD	260	2	50	0.33	Yes	1Φ /LCL-S
C8 [10]	Trapez. Solenoid	Trapez. Solenoid	450	45	85	0.52	Yes	1Φ /SS
C9 [11]	Rect. D-Helix	Planar Rect.	252	5	60	0.27	Yes	1Φ /SS

SP: Series-Parallel, SS: Series-Series, LCC: Inductor-Capacitor-Capacitor, LCL-S: Inductor-Capacitor-Inductor-Series

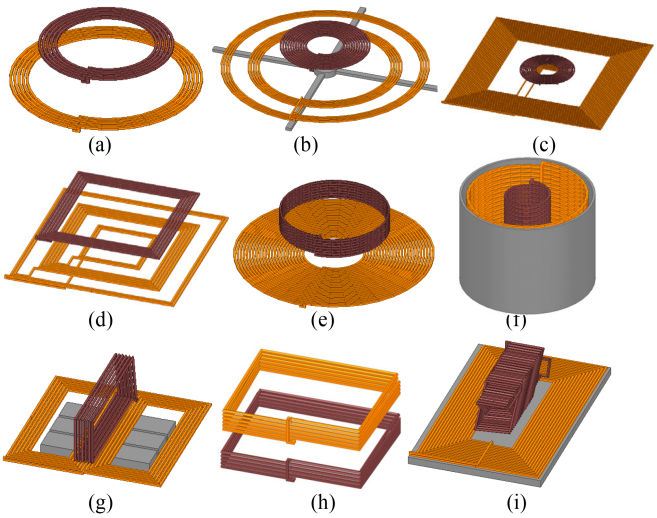

FIGURE 2. UAV Couplers (C) with both transmitter coil (orange colour) and receiver coil (brown colour) (a) Coupler 1 (C1), (b) Coupler 2 (C2), (c) Coupler 3 (C3), (d) Coupler 4 (C4), (e) Coupler 5 (C5), (f) Coupler 6 (C6), (g) Coupler 7 (C7), (h) Coupler 8 (C8), (i) Coupler 9 (C9).

the type of UAV and landing gear, the airgap or transmission distance varies from 2–200 mm. The range of operating frequency observed with existing couplers is 50–1000 kHz. In UAV applications, the placement of the *Rx*-coil depends on the UAV's size and the type of landing gear.

Fig. 2 shows the magnetic couplers (C) proposed for wireless charging of UAVs. The transmitter is shown in orange colour, while the brown colour shows the receiver coils. Magnetic couplers with planar *Rx*-coils are the most common and are illustrated in Fig. 2(a)–(d). Coupler 1 (C1) shown in Fig. 2(a) was designed to generate a low magnetic field so that electromagnetic interference does not affect the UAV's electronics [4]. Coupler 2 (C2), Coupler 3 (C3), and Coupler 4 (C4) shown in Fig. 2(b)–(d) were designed to achieve a high misalignment tolerance by extending the *Tx*-coil in the horizontal direction. The extended *Tx*-coil is a common design practice when trying to increase the misalignment tolerance [2], [5], [6].

Magnetic couplers with non-planar *Rx*-coils are illustrated in Fig. 2(e)–(i). Coupler 5 (C5), as shown in Fig. 2(e), uses a circular solenoid coil placed under a small UAV's base [7]. Coupler 6 (C6), as shown in Fig. 2(f), was designed for the tripod-legged landing gear common in large UAVs. The design has a reduced leakage magnetic field with minimal electromagnetic interference by implementing a three-phase IPT system, which was able to reduce the 7th and 11th harmonics in the *Tx* current [8]. Coupler 7 (C7), as shown in Fig. 2(g), was designed for the U-shaped landing gear with the goal of reducing the leakage magnetic field and maximizing efficiency [9]. These landing gears are common in small to medium-sized UAVs. Finally, Coupler 8 (C8) and Coupler 9 (C9), as shown in Fig. 2(h) and (i), were designed for larger UAVs [10], [11]. The *Rx*-coil in C9 is suited for either the T-shaped or U-shaped landing gear. It is evident from Table 2 that design specifications and operating conditions differ for each coupler. Furthermore, design parameters like transmission distance are a function of coil placement in relation to the landing gear. Therefore, before the comparative analysis begins, it is important to classify each coupler into a category of landing gear for which it is best suited. Based on the geometries of C1-5, these are best suited for small to medium-sized UAVs with short-legged landing gears [2], [4], [5], [6], [7]. In this case, the receiver is typically placed under the base of the UAV, resulting in a transmission distance of around 50mm [5]. C5-9 utilizes the landing gear of the UAV for the placement of the receiver coil. C6 is best suited for tripod-shaped landing gears. The *Rx*-coil fits around an extended leg of the landing gear and aligns with the *Tx*-coil when the UAV lands. C7 is best suited for U-shaped landing gears due to the shape of the *Rx*-coil, allowing it to fit directly on the leg. C8 is suitable for UAVs with larger landing gears. C9 is suitable for both U-shaped and T-shaped landing gears since the *Rx*-coil fits around the bottom of the leg. Due to the placement of the *Rx*-coils in C5-C9 relative to the *Tx*-coil, the resultant transmission distance is very small, approximately 10mm. It is evident that the size of the UAV and the type of landing gear influence the choice of coil geometry to be used. In addition, the transmission distance varies amongst these geometries. Thus, Section III highlights characteristics and considerations with respect to magnetic coupler and power electronics design as well as introduces related design parameters and constraints used in this analysis.

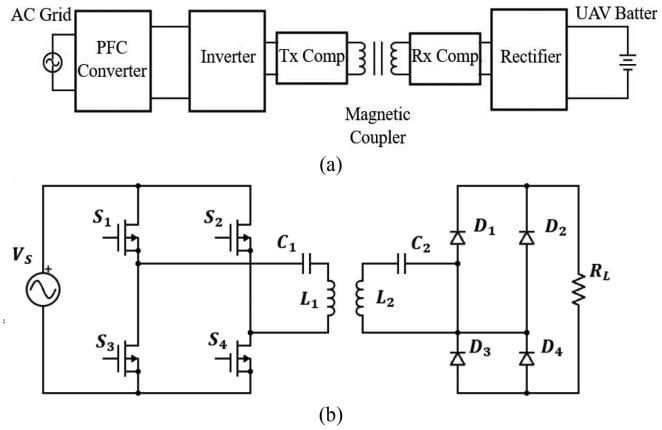

FIGURE 3. Inductive power transfer system. (a) Schematic diagram of IPT-based UAV chargers, (b) Circuit diagram of an SS-compensated IPT system.

TABLE 3. Design Parameters and Constraints

Variable	Value	Description
A_{max}	150x150mm	Maximum Coil Size
w_d	2.3mm	Wire Diameter
w_s	2mm	Wire Spacing
δ	10-50mm	Transmission Distance
P_{out}	252W	Required Output Power
Q_e	3-5	External Quality Factor
f_0	50-200kHz	Frequency
I_{max}	16.9A	Maximum Current

III. IPT SYSTEM DESIGN

A block diagram of a typical IPT system is illustrated in Fig. 3(a). It consists of an ac-dc converter with power factor correction (PFC), an inverter, primary and secondary side resonant compensation networks, the magnetic coupler consisting of the *Tx* and *Rx*-coils, a rectifier circuit and the load. In this article, the load is identified as a 10000mAh battery with a nominal voltage of 25.2 V. Both the magnetic coupler and the power electronics system should be considered in IPT design.

A. MAGNETIC COUPLER CHARACTERISTICS

1) COIL GEOMETRY

The magnetic coupler consists of the Tx-coil and Rx-coil. Since the receiver is important in UAV applications, a maximum coil size of 150 × 150 mm is defined for the Rx-coil. Additionally, a wire spacing (w_s) of 2 mm, and a wire diameter (w_d) of 2.3mm is selected for the analysis in this article for all the receivers and trasmitters. The detailed reason for selecting this wire diameter is provided in Section IV-A. The transmission distance (δ) is 10–50 mm. These values are summarised in Table 3.

2) COIL-TO-COIL EFFICIENCY

The maximum power transfer efficiency (PTE) of a magnetic coupler using an SS compensation is defined as:

$$\eta = \frac{k^2 Q_T Q_R}{\left(1+\sqrt{1+k^2 Q_T Q_R}\right)^2} \tag{1}$$

where Q_T and Q_R are the quality factors of the *Tx* and *Rx*-coils respectively. However, (1) assumes the losses in ferrite core are small compared to the losses in copper winding [17]. To accurately calculate the maximum efficiency of the coupler, the power loss due to copper winding and ferrite core material is considered. Copper losses are calculated by obtaining the series resistance of the windings:

$$P_{cu} = I_{RMS}^2 R_{ac} \tag{2}$$

where R_{ac} is the ac resistance of the wire, and it takes into consideration both skin and proximity effects. I_{RMS} is the rms current through the coils at resonant frequency. Litz wires are generally used for coils. Finite element analysis software such as ANSYS Maxwell can be used to derive R_{ac} by incorporating wire diameters and the number of strands in the litz wire. Power loss in ferrite core is calculated using the Steinmetz equation and integrating it over the core volumes [18]:

$$P_{fe} = \kappa f_0^{\alpha} \hat{B}^{\beta} \tag{3}$$

where, κ, α and β are the Steinmetz coefficients for magnetic materials, f_0 is the operating frequency, and $\hat{B}$ is the peak magnetic flux density. The Steinmetz coefficients for magnetic materials are available on manufacturer datasheets. Therefore, the total output power and coil-to-coil efficiency of a wireless power transfer coupler is given by:

$$P_{out} = P_{in} - P_{cu} - P_{fe} \tag{4}$$

$$\eta_c = \frac{P_{out}}{P_{in}} \tag{5}$$

Power loss due to shielding is not included since shielding methods are not common in UAV applications, according to the literature. Because the introduction of passive shielding will further increase the receiver's weight.

3) POWER DENSITY

It is desirable to increase the area-related power density (α_A) and volumetric power density (α_V) given by (6) and (7) of a coupler [17].

$$\alpha_A = \frac{P_{out}}{A_c} \tag{6}$$

$$\alpha_V = \frac{P_{out}}{V_c} \tag{7}$$

where A_c and V_c are the surface area and volume of the coil. α_A is mostly used for planar coils. However, α_V is a more useful performance index when considering non-planar coils. Therefore, α_V is considered in this analysis.

4) LEAKAGE MAGNETIC FIELD

The leakage magnetic field of a magnetic coupler is determined at a point in 3D space and is given by:

$$B_{Lf} = \left(B_x^2 + B_y^2 + B_z^2\right)^{\frac{1}{2}} \tag{8}$$

where B_x, B_y and B_z is the magnetic field density in the x, y and z directions. Leakage magnetic field should be minimized for increased coupler performance and to avoid EMI and exposure to surroundings [17].

5) MISALIGNMENT TOLERANCE

In UAV applications, positioning errors may occur in GPSs and cameras, which can cause misalignment between the *Tx* and *Rx*-coils when the vehicle lands. This reduces the mutual inductance (M) which reduces system stability and power transmission capability. Thus, M should be stable to ensure efficient power transfer. Misalignment tolerance is defined as the ratio of the maximum tolerable distance whereby M remains constant [5].

6) WEIGHT AND COST

Factors that typically contribute to the weight of a design is the volume of litz wire, ferrite core and passive shield. The cost of a magnetic coupler is also an important factor to consider in relation to weight. Hence, the number of materials used for the design of a coupler should be minimized. In UAV applications the weight of the *Rx*-coil should be minimized. Weight of the *Rx*-coil is therefore considered in this article.

B. POWER ELECTRONICS CONSIDERATION

The choice of power converters and compensation method impacts the overall performance of an IPT system. This article uses a resonant single-phase converter and class D rectifier. To maximize the efficiency of the IPT system, primary and secondary compensation is typically required. Compensation topologies minimize input apparent power and, therefore, maximize power transfer capability. In addition, they help achieve soft switching of semiconductor switches [19]. There are four basic compensation topologies i.e., Series-Series (SS), Series-Parallel (SP), Parallel-Series (PS), and Parallel-Parallel (PP). Table 2 shows that the compensation topology most commonly used for UAV charging applications is the SS topology. It exhibits a high efficiency for shorter transmission distances [20]. An SS topology can achieve a single zero-phase angle frequency (ZPAF), ensuring the system operates at a unique frequency. Therefore, the frequency splitting phenomenon or bifurcation, which is categorized by multiple ZPAF between the input voltage and current, can be avoided. Additionally, this can be achieved while maintaining a constant current output required for battery charging [19]. For these reasons, the SS topology is adopted for this analysis. Fig. 3(b) shows the circuit diagram for an SS-compensated IPT system. $S_1 - S_4$ are switches while $D_1 - D_4$ are diodes. L_1 and L_2 are the inductance of the transmitter and receiver coils. C_1 and C_2 are the series connected compensating capacitances on the transmitter and receiver sides.

1) INVERTER CURRENT HARMONICS

The non-linear nature of power converters can cause current harmonic distortion on the transmitter and receiver side, which can cause EMI with other electronic devices [10]. Current harmonic distortion in the inverter circuit can be minimized by ensuring a single ZPAF. Operating with ZPAF is also characterized as a bifurcation-free region. Therefore, designing for bifurcation-free operation by ensuring ZPAF will minimize inverter current harmonics [21]. For the SS compensated system, given the load requirements, the equivalent ac resistance of the UAV battery can be calculated as:

$$R_{eq} = \frac{8}{\pi^2}\left(R_{Ldc}\right) \tag{9}$$

where R_{Ldc} is the DC resistance of the battery. Thus, the DC load of 2.52 Ω in this article is modelled as the equivalent AC load resistance of 2.04 Ω for all couplers. In hardware implementation, the external quality factor (Q_e) of an IPT system is generally constrained to ensure system stability and improve efficiency. This is given by:

$$Q_e = \frac{\omega_0 L_2}{R_{eq}} \tag{10}$$

where $\omega_0 = 2\pi f_0$ is the chosen operating frequency and L_2 is the *Rx*-coil inductance [21]. The external quality factor (Q_e) in (10) of a coupler is also related to the critical coupling coefficient (k_c):

$$k_0 \ll k_c \approx \frac{1}{Q_e} \tag{11}$$

Therefore, if the coupling coefficient (k_0) and *Rx*-coil inductance (L_2) is known, then a suitable Q_e can be chosen to ensure k_0 is less than k_c. This design consideration ensures the IPT system operates in the bifurcation-free region [22]. Operating above the frequency corresponding to the chosen Q_e will violate (11), resulting in k_0 exceeding k_c, thus bifurcation may occur. Equation (10) is dependent on the *Rx*-coil inductance; hence the operating frequency and external quality factors of each design will differ.

2) RECTIFIER CURRENT HARMONICS

To reduce current harmonics in the receiver current due to non-linearities in the class D rectifier circuit, the existing couplers are required to satisfy the condition below [21]:

$$Q_e \geq 3 \tag{12}$$

This suggests that for an SS compensated system, the coupling coefficient (k_0) should not exceed 0.33. A strong coupling would require a lower constraint on Q_e or $Q_e < 3$ to avoid bifurcation. This violates (12). Furthermore, in light load applications such as the one in this article, bifurcation is more likely to occur when there is strong coupling between the *Rx* and *Tx*-coil [23]. Thus, (11) and (12) should be satisfied,

and over-coupling should be avoided to reduce *Tx* and *Rx* side THD in light-load SS-compensated IPT systems [24]. To ensure these conditions are followed, the Q_e is constrained to 3-5 in this analysis.

3) CURRENT AND VOLTAGE EQUATIONS FOR SS TOPOLOGY

Given the inductances of the *Tx*-coil (L_1) and *Rx*-coil (L_1) and the operating frequency (f_0), the primary and secondary series compensating capacitors can be calculated independent of the coupling coefficient (k_0):

$$C_1 = \frac{1}{\omega_0^2 L_1} \tag{13}$$

$$C_2 = \frac{1}{\omega_0^2 L_2} \tag{14}$$

The reflected impedance from the secondary side and the primary and secondary current is given by [25]:

$$Z_r = -j\omega I_2 = \frac{(\omega M)^2}{Z_2} \tag{15}$$

$$I_1 = \frac{V_s}{Z_1 + Z_2} = \frac{Z_2 V_s}{Z_1 Z_2 + (\omega M)^2} \tag{16}$$

$$I_2 = \frac{j\omega M I_1}{Z_2} = \frac{j\omega M V_s}{Z_1 Z_2 + (\omega M)^2} \tag{17}$$

where $Z_1 = j\omega L_1 + \frac{1}{j\omega C_1} + R_1$, and $Z_2 = j\omega L_2 + \frac{1}{j\omega C_2} + R_2 + R_{eq}$. Since the load is a battery with a nominal voltage and a constant charging current, (15)–(17) can be simplified to the following provided the IPT system operates at the resonant frequency.

The secondary or load voltage and current are determined using the battery specifications and are given by [26]:

$$V_2 = \left(\frac{4}{\pi}\right)(V_{dc}) \tag{18}$$

$$I_2 = \frac{V_2}{R_{eq}} \tag{19}$$

The supply voltage needed to achieve the load requirements and the primary current in the *Tx*-coil is given by [26]:

$$V_S = I_2 \omega_0 M \tag{20}$$

$$Z_r = \frac{\omega_0^2 M^2}{R_{eq}} \tag{21}$$

$$I_1 = \frac{V_S}{Z_r} \tag{22}$$

Finally, the voltage gain in an SS topology is given by [25]:

$$G = \left|\frac{V_L}{V_s}\right| = \left|\frac{j\omega M R_{eq}}{Z_1 Z_2 + (\omega M)^2}\right| \tag{23}$$

Given the load or battery specifications, the theoretical values of the peak load voltage and current can be calculated using (18) and (19) and is common for all couplers at 32.09 V and 15.73 A. For an SS compensated IPT system, the supply voltage (V_S), and primary current (I_1) is dependent on the load requirements and the relationship between the operating frequency (f_0), and mutual inductance (M). Therefore, the current flowing in the *Tx*-coil is influenced by the choice of frequency. For the chosen diameter of copper wire (w_d) the peak current in the coils should not exceed 16.9 A. Therefore, a suitable frequency should be selected for each coupler while considering their respective Q_e. The operating frequency of all couplers in this analysis is constrained to [50; 200 kHz]. According to Table 2, this range of frequency is common in UAV applications, and constraining the operating frequency ensures that switching losses in power electronics are kept to a minimum within this range. By following (13)–(22), each coupler is designed to transfer 252 W power to the load. Moreover, all designs meet the constraints defined by (11) and (12) by selecting an appropriate operating frequency with the range of 50 kHz to 200 kHz to ensure bifurcation-free operation and to reduce harmonic currents. The complete set of design parameters and constraints of this article are summarised in Table 3.

IV. DETAILED ANALYSIS AND RESULTS

Analysis of existing couplers was carried out using ANSYS Maxwell3D and MATLAB. Each couplers' secondary inductance (L_2) was designed by considering the constraint on Q_e and f_0 and the transmission distance was chosen such that coupling coefficient (k_0) remains below critical coupling (k_c). In addition, mutual inductance (M) needed to be properly designed so that the constraint on I_1 is followed. The physical and electromagnetic properties of the couplers post-simulation are illustrated in Table 4. These include transmission distance, weight, operating frequency (f_0), external quality factor (Q_e), primary (L_1), and secondary (L_2) inductance, mutual inductance (M), primary (R_1), and secondary (R_2) coil resistances and coupling coefficient (k_0).

A. OUTPUT POWER AND COIL-TO-COIL EFFICIENCY

The output power and coil-to-coil efficiency were acquired by exciting each coil with the respective currents determined by (19) and (22) and interpreting the post-simulation results. To model the loss due to ferrite, material properties of ferrite core 3C90 were inserted in the core loss setting. Accurate calculation of the power loss matrix is achieved by inserting the Steinmetz coefficients for ferrite from (3). Copper losses are obtained from the stranded loss matrix in ANSYS and are governed by (2), and includes the impact of proximity and skin effects. Thus, (4) and (5) determined the output power and coil-to-coil efficiency. The primary (I_1), secondary currents (I_2) and respective current densities (J_x), copper (P_{cu}), and ferrite (P_{fe}) losses, output power (P_{out}), and efficiency (η_c) of each coupler are given in Table 5. Copper losses are a function of the *Tx* and *Rx*-coil resistances (R_1 and R_2) and the primary and secondary currents (I_1 and I_2). Owing to the SS compensation topology, which allows constant output current for a given power rating (250W in this application), the secondary current (I_2), and therefore the current density

TABLE 4. Properties Of Simulated Couplers

Coupler (C)	Distance (mm)	Weight (g)	f_0 (kHz)	Q_e	$L_1(\mu H)$	R_1(mΩ)	$M(\mu H)$	$L_2(\mu H)$	R_2(mΩ)	k_0
C1	40	92.39	200	3.02	4.91	9.38	1.51	4.91	6.32	0.33
C2	40	179	75	3.44	14.86	26.47	5.26	14.86	12.23	0.29
C3	10	178.83	110	4.77	14.07	112.46	10.36	14.07	12.23	0.20
C4	50	144.72	122	3.02	8.03	18.59	3.10	8.03	9.98	0.33
C5	40	158	90	3.16	11.35	42.33	8.71	11.35	10.89	0.32
C6	30	116.3	184	3.01	5.32	21.19	4.18	5.32	8	0.33
C7	10	118.62	160	3.01	6.11	19.35	3.48	6.11	8.19	0.33
C8	20	128.07	160	3.36	6.81	10.38	2.01	6.81	8.83	0.30
C9	10	370.10	72	3.77	16.99	34.07	9.85	16.99	25.42	0.27

TABLE 5. Efficiency and Current Density Of Simulated Couplers

Coupler (C)	I_1 (A)	J_1 (A/mm^2)	$P_{cu_{Tx}}(W)$	I_2 (A)	J_2 (A/mm^2)	$P_{cu_{Rx}}(W)$	$P_{cu}(W)$	$P_{fe}(mW)$	$P_{out}(W)$	η_c
C1	16.9	3.19	2.68	15.7	2.97	1.56	4.24	-	247.76	98.32
C2	12.9	2.44	4.4	15.7	2.97	3.01	7.45	287.5	244.26	96.93
C3	4.5	0.85	2.28	15.7	2.97	3.01	5.28	-	246.72	97.91
C4	13.5	2.55	3.39	15.7	2.97	2.46	5.85	-	246.15	97.68
C5	6.5	1.23	1.79	15.7	2.97	2.68	4.48	-	247.52	98.22
C6	6.6	1.25	0.92	15.7	2.97	1.97	2.92	59.6	249.03	98.82
C7	9.2	1.74	1.64	15.7	2.97	2.02	3.65	62.9	248.29	98.53
C8	15.9	3.01	2.62	15.7	2.97	2.18	4.8	-	247.2	98.11
C9	7.2	1.36	1.77	15.7	2.97	6.27	8.04	23.2	243.94	96.80

in the *Rx*-coil (J_2) of each coupler is similar according to (18) and (19). As seen from Table 5, the maximum value of current in *Rx*-coil is 15.7 A, and therefore a Litz wire consisting of 200 strands and a diameter of 2.3 mm is used for modelling the receiver coils. Current in the *Tx*-coils (I_1) depends on the relationship between mutual inductance (M) and operating frequency (f_0), as shown by (20)–(22). The mutual inductance varies with different coupler structures, and a suitable operating frequency within the range of 50kHz-200kHz must be selected for each coupler to satisfy the constraints (11), and (12). Therefore, *Tx*-coil current (I_1) varies. A high primary current is observed for low mutual inductances. However, the maximum current observed in the *Tx*-coil is 16.9A, as shown in Table 5. This current is within the current handling capability of the copper wires used for analysis. The couplers have a high maximum coil-to-coil efficiency, with C1, C6, and C7 having the highest due to lower losses in the coil windings. C2 and C9 have the lowest coil-to-coil efficiency. The effect of coil-to-coil efficiency and output power with changing load conditions are shown in Fig. 4. Efficiency reduces when the load resistance reduces and output power is low, and improves when the load resistance increases and output power is high. This behaviour is inherent in SS-compensated IPT systems, as discussed in the literature [25]. Therefore, the SS topology achieves maximum efficiency for high-power applications characterized by a larger load.

Since each coupler is operating at different frequencies, the power loss in the full-bridge inverter and single-phase rectifier cannot be ignored. The power loss in each MOSFET of the full bridge inverter is the sum of the conduction loss (P_d), switching loss (P_{sw}), output loss (P_o), gate drive loss (P_g) and body diode loss (P_b). These losses are given by (24)–(28) [27].

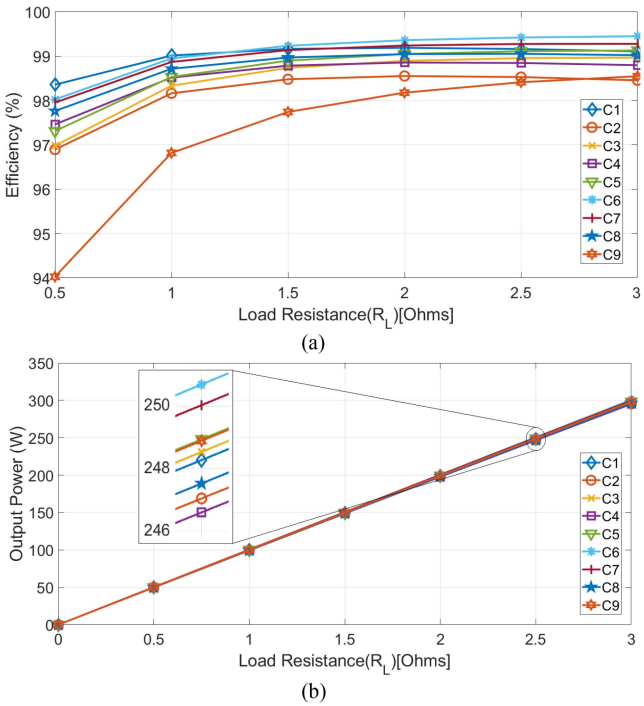

FIGURE 4. (a) Efficiency versus load resistance (b) Output power versus load resistance.

$$P_d = \left(\frac{P_{in}}{V_{in}}\right)^2 \times TCR \times R_{DS} \tag{24}$$

TABLE 6. Power Loss in Inverter and Rectifier

Coupler (C)	P_d	P_{sw}	P_{out}	P_g	P_b	P_{mosfet}	P_{inv}	P_{diode}	P_{cap}	P_{rect}
C1	5.26	4.81	0.08	0.423	0.41	10.98	43.94	8.77	0.35	36.48
C2	3.08	1.80	0.05	0.16	0.12	5.21	20.84	8.77	0.35	36.48
C3	0.37	2.65	0.08	0.23	0.06	3.39	13.56	8.77	0.35	36.48
C4	3.35	2.94	0.07	0.26	0.2	6.81	27.25	8.77	0.35	36.48
C5	0.78	2.17	0.04	0.19	0.07	3.24	12.97	8.77	0.35	36.48
C6	0.81	4.43	0.07	0.39	0.15	5.84	23.39	8.77	0.35	36.48
C7	1.55	3.85	0.09	0.34	0.18	6	24	8.77	0.35	36.48
C8	4.63	3.85	0.08	0.34	0.31	9.2	36.81	8.77	0.35	36.48
C9	0.99	1.73	0.03	0.15	0.06	2.97	11.88	8.77	0.35	36.48

$$P_{sw} = \frac{P_{in}}{2} \times \frac{Q_{sw}}{I_{g_{off}}} \times f_0 \tag{25}$$

$$P_o = \frac{V_{in}}{2} \times Q_{oss} \times f_0 \tag{26}$$

$$P_g = V_{dr} \times Q_g \times f_0 \tag{27}$$

$$P_b = \frac{P_{in}}{V_{in}} \times V_{fwd} \times t_{rr} \times f_0 \tag{28}$$

In (24)–(28), P_{in} and V_{in} is the input power measured before the inverter. The remaining variables are determined using the MOSFET datasheet. TCR is the temperature coefficient of resistance. R_{DS} is the drain-source resistance. Q_{sw} is the switching charge which is the addition of Q_{GS} (gate to source charge) and Q_{GD} (gate to drain charge). Q_{oss} is the output charge. V_{dr} is the output voltage of the gate driver which drives the MOSFET. Q_g is the total gate charge. V_{fwd} is the forward voltage drop of the MOSFET. T_{rr} is the reverse recovery time. The total loss in each MOSFET is given by (29) [27].

$$P_{mosfet} = P_d + P_{sw} + P_o + P_g + P_b \tag{29}$$

Table 6 shows the individual and total losses for each coupler analyzed in this article. The losses shown in Table 6 are calculated for the semiconductor devices used for experimental validation. In this article, the inverter comprises of four CoolMOSTM CFD7 MOSFETs, and losses are calculated assuming the same inverter is used for all the couplers. The conduction and switching losses are dominant components in the inverter power loss equation. The input voltage (V_{in}) is a function of the switching frequency (f_0) and the mutual inductance (M) of each coupler according to (20). Coupler structures with a higher mutual inductance (M) have a higher input voltage (V_{in}) which lowers the conduction losses (P_d) according to (24). Additionally, switching losses (P_{sw}) are greater in coupler structures with higher switching frequencies (f_0) according to (25).

Power loss in the single-phase rectifier is calculated using (30), which calculates the loss in each diode [28].

$$P_{diode} = \left(V_F \times I_F \times \frac{t_{on}}{t_{sw}}\right) + \left(V_R \times I_R \times \frac{t_{off}}{t_{sw}}\right) \tag{30}$$

Where the first term of (30) provides the diode's ON-state losses, while the second term provides the OFF-state losses. V_F is the forward voltage and I_F is the current flow during the ON-state. V_R is the reverse voltage and I_R is the current through the diode at this voltage. DSEP2X31-06A diodes were used in the rectifier, and the losses are calculated based on it. Since this article uses SS compensation, each coupler's output voltage and current are the same, resulting in equal rectifier losses. The losses are provided in Table 6. It is important to highlight that higher rectifier losses are observed due to high V_F in the selected diode and higher I_F or I_2, as seen in Table 5.

TABLE 7. Magnetic Coupler Performance Indices

Coupler (C)	α_v (kW/mm^3)	d_{BLf} (cm)	T (°C)	M_T (mm)
C1	23 956	22.2	25.5	90
C2	12 190	19	24.4	80
C3	12 324	31	26.8	40
C4	15 194	25.3	25.1	60
C5	13 994	24	25.2	40
C6	19 128	14	27.4	40
C7	18 699	5.5	26	30, 50
C8	17 243	21	25.2	70
C9	5 888	26.5	30	20, 60

B. POWER DENSITY, THERMAL ANALYSIS AND LEAKAGE FIELD

Using the output power and the volume of the *Rx*-coil extracted from ANSYS, the volumetric power density was determined with (7). Table 7 shows the power density (α_v) of all the couplers. A high output power and low *Rx*-coil volume resulted in high-power density coils. Since volume is a function of weight, lighter *Rx*-coils (i.e., low volume) such as C1, C6, and C7 have the highest power density. High power density coils are generally favourable however, high maximum coil-to-coil efficiency can still be achieved with lower power densities for UAV applications.

Furthermore, high power densities can result in higher temperature coils, leading to thermal losses [17]. A thermal analysis of each coupler is provided in Fig. 5. The Tx and Rx excitation currents provided in Table 5 are used for this analysis. Each temperature scale shows the temperature distribution of the coupler when transferring ~250 W-rated power using an SS-compensated IPT system. The analysis provides the temperature of the coils at a steady state, and Table 7 summarises the maximum steady-state temperature of the coupler.

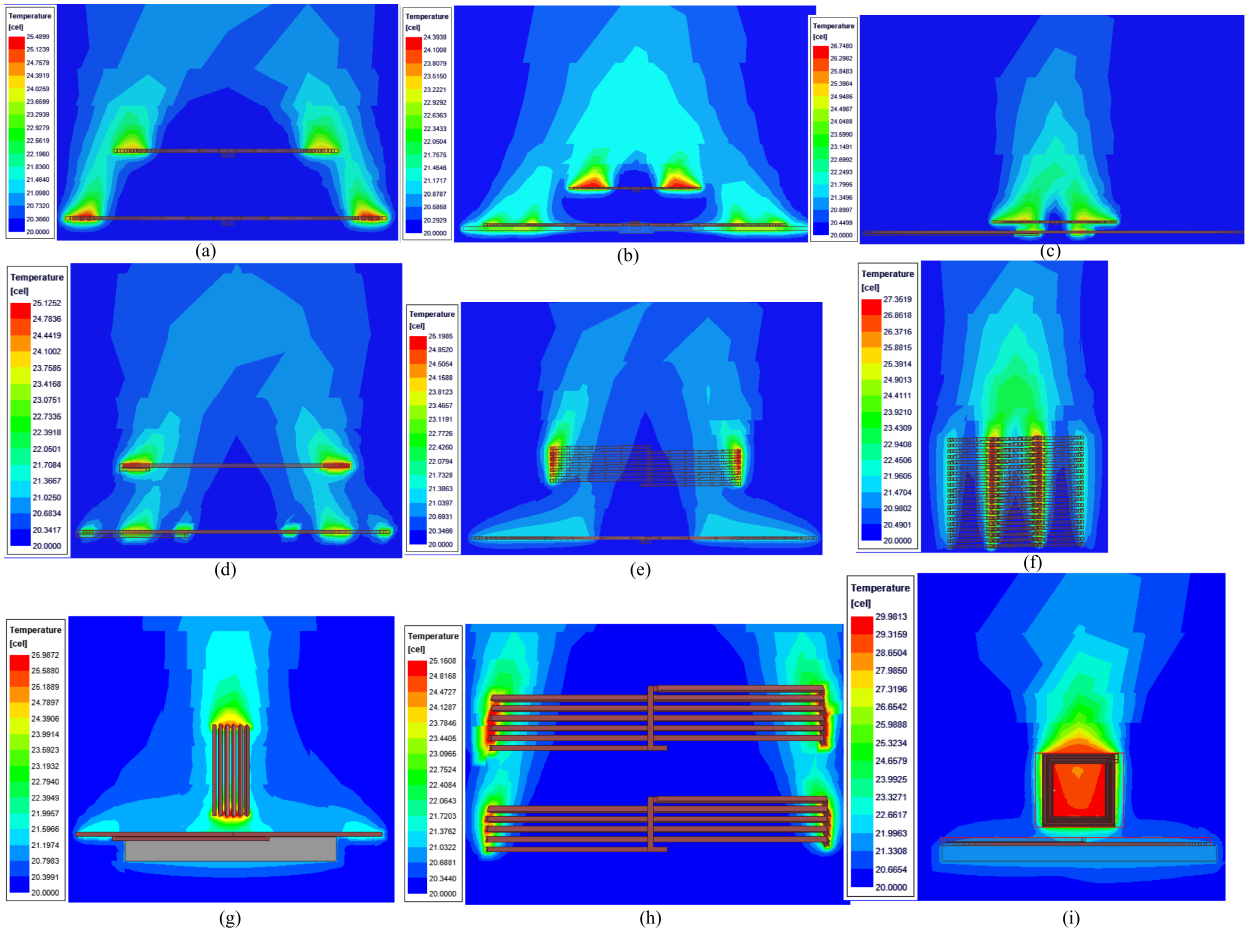

FIGURE 5. Thermal Analysis of Magnetic Couplers (C) (a) C1, (b) C2, (c) C3, (d) C4, (e) C5, (f) C6, (g) C7, (h) C8, (i) C9.

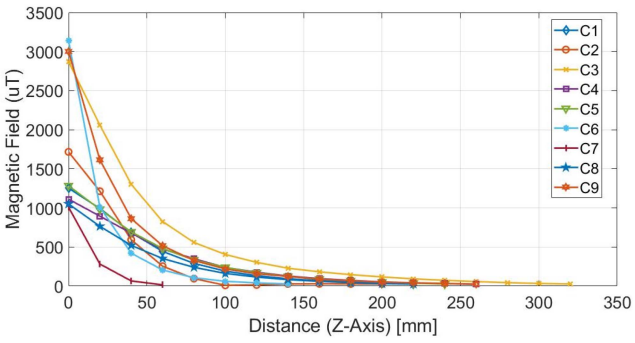

FIGURE 6. Leakage Field Behaviour of Couplers.

C9 has the highest temperature at steady state, followed by C6 due to the compact design of the coils. High temperatures are also a result of the higher number of turns relative to the rest of the couplers. Nevertheless, the maximum recorded steady-state temperature is 30 °C for C9; no forced cooling is required.

Leakage field analysis was carried out by measuring the magnetic field strength along the vertical distance until 27 μT was detected. This is illustrated in Fig. 6. It is desirable to consider the field in the vertical distance with respect to drone applications because IPT coils are typically placed beneath the drone electronics and motors. Leakage field can potentially interfere with the sensitive electronics of the UAV, causing electromagnetic interference (EMI). It is shown that all couplers exhibit similar behaviour for the leakage field. C6 and C9 have a higher initial field at 0 mm due to ferromagnetic material strengthening the field. C4, C7, and C8 have a low initial field at 0 mm. The field strength of C4 and C8 at this point is low due to a lower number of turns. C7 has a lower field in the vertical axis due to the orientation of the *Rx*-coil and the direction of the field produced by that coil. The distance (d_{BLf}) in which the field meeting 27μT is given in Table 7. This distance is lowest for C6 and C7, indicating a lower leakage field for these couplers and desirable for applications where EMI is a major design criterion.

C. MUTUAL INDUCTANCE AND MISALIGNMENT TOLERANCE

By observing the variation in mutual inductance with respect to lateral (y-axis) and longitudinal (x-axis) misalignments, the tolerance of each coil to misalignments is obtained. The maximum distance over which mutual inductance remains

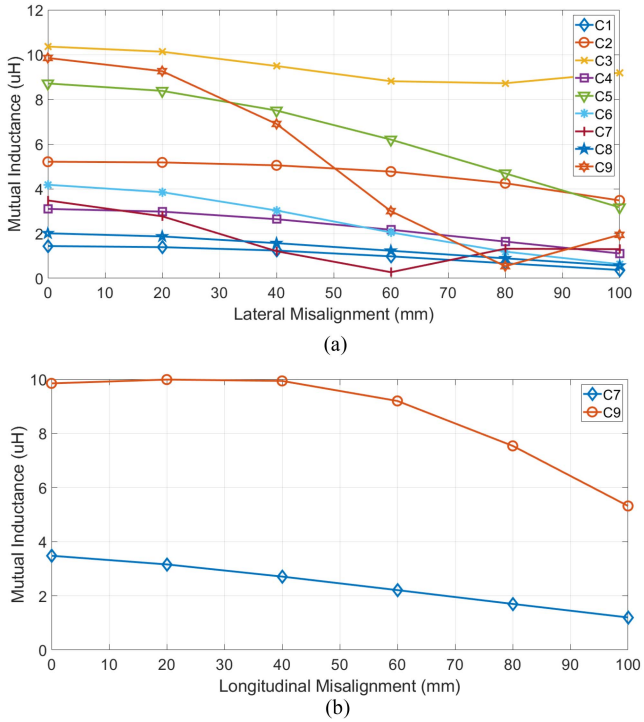

FIGURE 7. Mutual Inductance versus (a) Lateral Misalignment and (b) Longitudinal Misalignment.

TABLE 8. Impact of Mutual Inductance on Primary Current and Voltage

Coupler (C)	$M_{30\%}(\mu H)$	$Vin\ (V)$	$Vin_{30\%}\ (V)$	$I_1(A)$	$I_{1\ 30\%}(A)$
C1	1.06	23	33	17	24
C2	3.68	31	44	13	18
C3	7.25	88	126	4	6
C4	2.17	29	42	14	19
C5	6.10	61	87	7	9
C6	2.93	60	85	7	9
C7	2.44	43	62	9	13
C8	1.41	25	36	16	23
C9	6.90	55	78	7	10

TABLE 9. Total Harmonic Distortion and Voltage Gain

Coupler (C)	$THD(I_{Tx})$	$THD(I_{Rx})$	V_G
C1	2.77	4.56	1.07
C2	2.53	3.93	0.82
C3	1.78	2.74	0.28
C4	3.73	4.71	0.85
C5	3.63	4.46	0.41
C6	4.59	4.86	0.42
C7	3.89	4.74	0.58
C8	3.72	4.21	1.01
C9	3.46	3.67	0.46

stable (variation of $\pm 1\mu H$) is considered the tolerance of a coupler. The variation of mutual inductance versus lateral and longitudinal misalignment is illustrated in Fig. 7, and the misalignment tolerance (M_T) is provided in Table 7. By observing how stable mutual inductance is with respect to misalignment, it is evident that C1, C2, C8, and C4 have the highest tolerance to misalignment since the *Tx* and *Rx*-coils are geometrically similar. Additionally, C2 and C4 have extended *Tx*-coils which has been found to improve tolerance to misalignment [2], [6]. C7 and C9 have the lowest tolerance in the lateral direction but a high tolerance to longitudinal misalignment due to the shape of the *Rx*-coil in relation to the *Tx*-coil.

According to (20)–(22), a change in mutual inductance caused by misalignments can impact the primary side voltage and current. It is known that when misalignment occurs, the mutual inductance reduces. To compensate and transfer the required power to the load, the primary voltage and current need to increase, causing strain on the power electronics and reducing the efficiency of the IPT system. Additional analysis is performed for each coupler to identify the impact on power electronics, particularly the DC supply voltage and the peak primary current when the mutual inductance decreases by 30%. The 30% reduction in mutual inductance ($M_{30\%}$), the DC supply voltage ($Vdc_{30\%}$), and the peak primary current ($I_{1\ 30\%}$) at the reduced mutual inductance is illustrated in Table 8 alongside the original values. Results show that when mutual inductance (M) decreases, the DC supply voltage (Vdc) and peak primary (I_1) current increases proportionally. Thus, couplers with high tolerance to misalignment are favorable in UAV applications to avoid electric strain on the supply.

D. POWER ELECTRONICS ANALYSIS

To understand how each magnetic coupler operates, further analysis of the power electronics is required. The total harmonic distortion in *Tx and Rx* currents is considered a performance index and calculated using MATLAB Simulink and is provided in Table 9. It is evident that the external quality factor (Q_e) of an IPT system influences the current distortion in the coils. The correlation between Q_e and THD shows that a higher Q_e, resulting in lower THD in both *Tx* and *Rx* currents, thereby reducing harmonics in both the inverter and rectifier circuits. The values used in this analysis are provided in Table 4. Additionally, since Q_e is constrained between 3-5 in this article, the distortion in both *Tx* and *Rx* currents in all couplers is below 5%. The analysis showed C2, C3, and C9 having the lowest distortion in *Rx* current, and C1, C2, C3, and C9 have the lowest distortion in *Tx* current due to higher external quality factors.

The DC voltage gain (V_G) of each coupler is calculated using (23) and is also provided in Table 9. In an SS topology, voltage gain is dependent on mutual inductance and frequency. It is observed that the voltage gain is higher in couplers with lower mutual inductances. It has also been discussed that a lower mutual inductance requires a higher input current for the same load. Thus, a high voltage gain is observed. Couplers with a low DC voltage gain indicate that a high input voltage is required to meet the output voltage

TABLE 10. Overall Performance of Magnetic Couplers

Coupler (C)	Efficiency (%)	VP. Density (W/m^3)	Leakage Field (cm)	Mis. Tolerance (mm)	Weight(g)	THD (I_{Rx})	THD(I_{Tx})
C1	98.32	23 956 088	22.2	90	92.39	4.56	2.77
C2	96.93	12 189 619	19	80	179	3.93	2.53
C3	97.91	12 324 324	31	40	178.83	2.74	1.78
C4	97.68	15 194 247	25.3	60	144.72	4.71	3.73
C5	98.22	13 993 756	24	40	158	4.46	3.63
C6	98.82	19 127 896	14	40	116.3	4.86	4.59
C7	98.53	18 698 691	5.5	30, 50	118.62	4.74	3.89
C8	98.11	17 243 124	21	70	128.07	4.21	3.72
C9	96.80	5 887 847.6	26.5	20, 60	370.10	3.67	3.46

VP. Density: Volumetric Power Density, Mis. To

of 25.2V. The low voltage gain is also due to a lower input current.

E. OVERALL SCORE AND WEIGHTING

To evaluate the performance of each coupler studied in this article, a ranking and scoring method is used. The procedure used in this article is the Rank Order Centroid (ROC), which uses a conversion formula to apply a weight to the performance index based on its importance. The equation is provided below [29]:

$$W_i = \left(\frac{1}{M}\right)\sum_{n=i}^{M}\frac{1}{n} \tag{31}$$

where M is the number of performance indices considered and W is the weight for the ith index.

Couplers are given a score for their performance in each criterion. The highest score a coupler can achieve is 9, and the lowest score is 1. A weight is then applied to these scores depending on the criteria. To calculate the weights of each index, five scenarios are considered where specific indices are given more importance than others. The first scenario considers all indices equal and applies an equal weighting to all. Efficient power transfer and weight of the *Rx*-coil are significant in UAV applications [1]. Therefore, the second scenario has those two indices carrying the highest weighting while the remaining are given equal weighting. The third scenario includes misalignment tolerance as an equally important index compared to efficiency and weight, while the remaining are considered less important. Misalignment tolerance becomes important when considering the effect of reduced mutual inductance on the input power electronics. In the fourth scenario, the leakage field replaces misalignment tolerance. Industrial standards limit the leakage field and are not always considered a performance index. However, it is required to minimize the leakage field so that surrounding electronics and objects are not harmed. In the fifth scenario, THD replaces the leakage field. In UAV applications, sensitive electronics are in close proximity to the coupler. A high THD in the fundamental component can cause EMI, which may affect the functionality of the UAV. Therefore, minimizing THD is necessary in UAV applications.

TABLE 11. Overall Score of Couplers

Coupler (C)	Sc. 1	Sc. 2	Sc. 3	Sc. 4	Sc. 5
C1	50	7.7	7.75	6.99	6.9025
C2	36	3.1	4.44	4.25	4.9225
C3	32	3.875	3.82	3.44	5.2475
C4	28	4	4.34	3.77	3.745
C5	31	4.8	4.33	4.52	4.63
C6	38	7.425	6.08	7.03	5.0825
C7	37	6.725	5.45	6.78	5.0025
C8	42	5.675	5.94	5.75	5.8325
C9	20	1.65	1.77	1.96	3.32

In each scenario, there are always 2 sets of indices with equal weighting at any given time. Therefore, M is considered as two instead of seven different indices. Therefore, weights are divided into parts of 0.75 and 0.25 according to (24). For the scenario where two indices are highly important, 0.75 is separated into two parts, while 0.25 is separated into 5. For scenarios with three indices of high importance, 0.75 is divided into 3 equal parts, while 0.25 is divided into 4. Table 10 provides the overall performance of each coupler in terms of the performance indices. Table 11 provides the overall score based on the different scenarios. Considering Scenario 1, where each performance index is given equal weighting, C1 and C8 perform the best. In Scenario 2, C1, C6, and C7 perform best, with efficiency and weight as the highest weighted indices. The results of Scenario 3 indicate that C1 and C6 perform best with efficiency, weight, and misalignment tolerance as the highest weighted indices. In Scenario 4, C1 and C6 have the best performance. Finally, In Scenario 5, where THD is considered in addition to efficiency and weight as an important index, C1 and C8 perform best. Considering all scenarios, it is obvious that C1 and C6 stand out as the best overall performing couplers.

V. EXPERIMENTAL VALIDATION

The analysis in this article is carried out based on finite element analysis and MATLAB Simulink simulations due to its complexity. However, one of the couplers from the analysis is implemented, and its results are compared with the simulated results to validate the efficacy of the proposed analysis. C9 is realized in this article as the experimental analysis was not

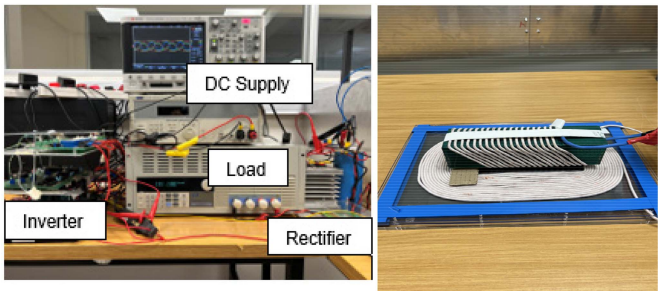

FIGURE 8. Hardware implementation (a) Experimental setup, (b) Fabricated coils.

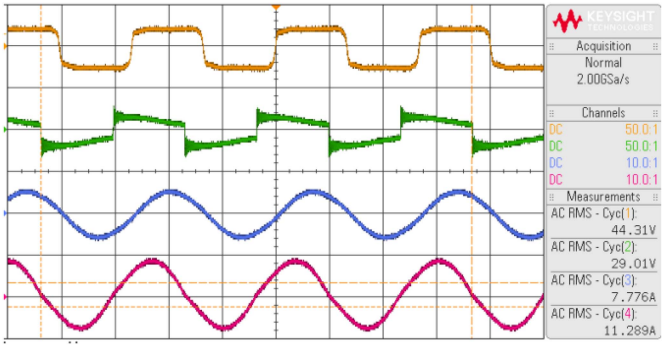

FIGURE 9. Input and output voltage and current waveforms.

TABLE 12. Coupler 9 Parameters

Parameter	Symbol	Sim.	Exp.	Δ error
T_x Inductance	L_1 (μH)	93.62	89.63	-3.99
R_x Inductance	L_2 (μH)	16.97	14.22	-2.75
Mutual Inductance	M (μH)	9.66	10.26	+0.6
Resonant frequency	f_0 (kHz)	72	74.5	+2.5
T_x Resistance	R_1 $(m\Omega)$	34.07	40	+5.93
R_x Resistance	R_2 $(m\Omega)$	25.42	37	+11.58
Coupling Coefficient	k_0	0.25	0.28	+0.03
Efficiency	η_c (%)	96.80	96.27	-0.53
Leakage Field	d_{BLf} (cm)	26.5	26.5	0
Temperature	T (°C)	30	30.9	+0.9
T_x Current Distortion	THD (I_{Tx})	3.46	4.32	+0.86
R_x Current Distortion	THD (I_{Rx})	3.67	5.09	+1.42
Inverter losses	P_{inv}	11.73	11.88	+0.15
Rectifier losses	P_{rect}	36.48	37.09	+0.61

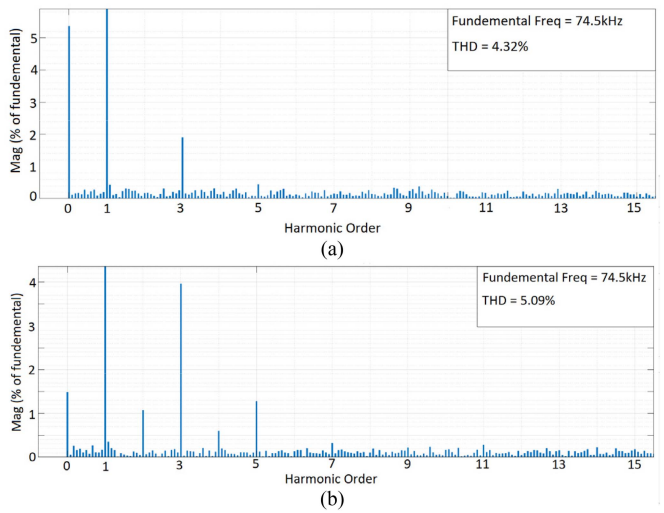

FIGURE 10. Total Harmonic Distortion in (a) *Tx* and (b) *Rx* current.

presented in the literature and is the only coil proposed for T-legged drones.

Fig. 8(a) shows the experimental setup of the IPT system where CoolMOSTM CFD7 power transistors are used in the inverters and DSEP2X31-06A fast recovery diodes are utilized in the rectifier. Switches are protected from high-frequency switching stresses by utilizing snubber capacitors across the DC bus. Compensation capacitors are realized using metalized polypropylene film capacitors. ELP/DCM9715 electronic load is used to model the battery or load of the UAV. The controller is implemented using a TI LaunchPad kit with C2000 F2837x MCU. Fig. 8(b) shows the fabricated C9. The diameter of copper wire is 2.3 mm, which consists of 200 strands of AWG38 wires. Ferrite with a permeability of 1680 is used for the core. Table 12 compares the parameters and performance indices of the simulated and experimental implementation of C9 and provides the error between both cases. The experimental setup achieved a coil-to-coil efficiency (η_c) of 96.27%. The efficiency deviation compared to simulations is 0.53, which is minimal and attests to the accuracy of the analysis. Losses in the inverter and rectifier for the simulated and experimental setup are also provided and have minimal error deviation which validates the accuracy of the analysis

The input and output voltage and current waveforms are shown in Fig. 9. Due to the low error in coil inductance and the minor increase in coupling of the fabricated coils, a higher operating frequency was chosen such that Q_e is constrained to 3.26 corresponding to a critical coupling of 0.31. Constraints (11) and (12) are still satisfied. The total harmonic distortion measured in the *Tx* and *Rx* current is 4.32% and 5.09% respectively, as shown in Fig. 10. A minor increase in THD is observed in the experimental setup because of the reduced Q_e compared to the simulated coils. The magnetic field generated by the fabricated coils in Fig. 11 was measured in the vertical (z-axis), lateral (y-axis) and longitudinal (x-axis) directions using Narda ELT-400. The field along the vertical axis match closely with the field analysis carried out in Section IV-B. The variation of mutual inductance (M) with misalignment in the simulated and fabricated coils are compared in Fig. 12 and are almost identical. Efficiency with respect to misalignment is illustrated in Fig. 13. Efficiency with respect to variation in load resistance is illustrated in Fig. 14. The experimental coil-coil efficiency measurement includes the losses in the capacitors

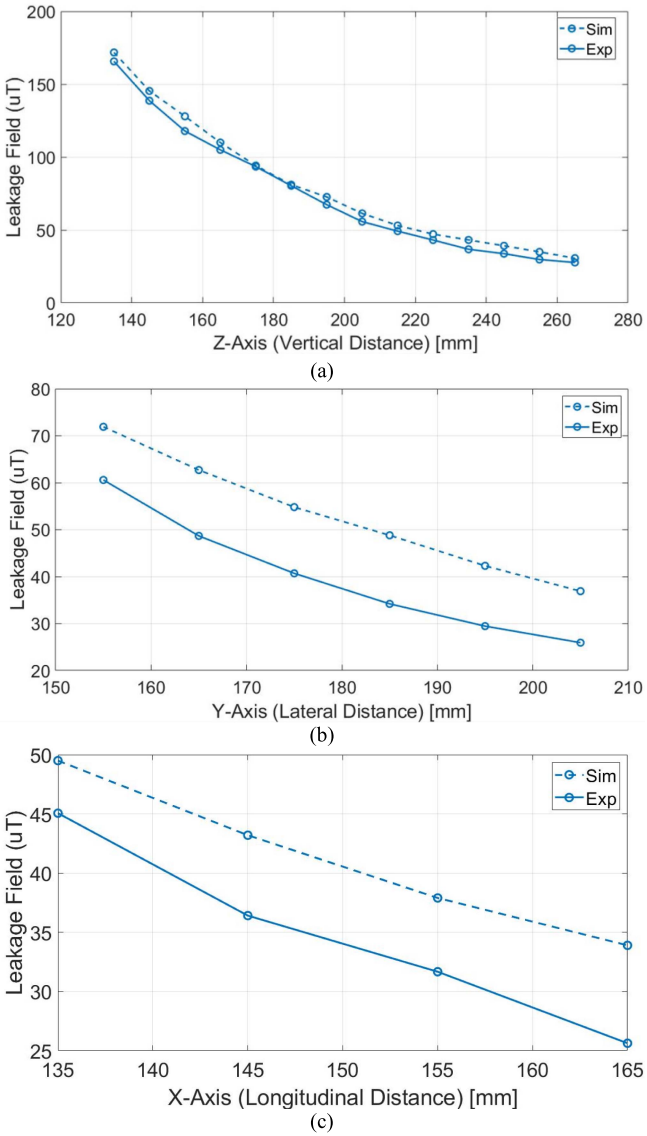

FIGURE 11. Leakage Field Analysis of C9 (a) Z-Axis (b) Y-Axis (c) X-Axis.

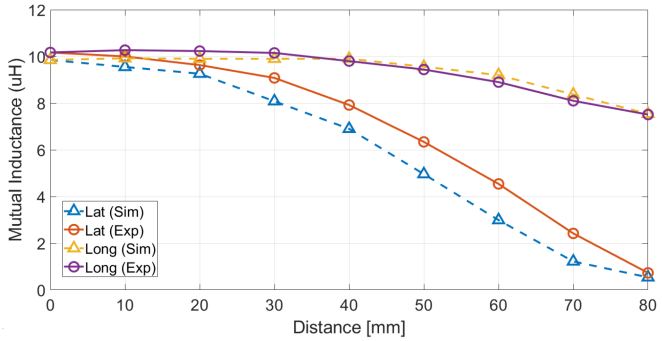

FIGURE 12. Mutual Inductance versus Misalignment.

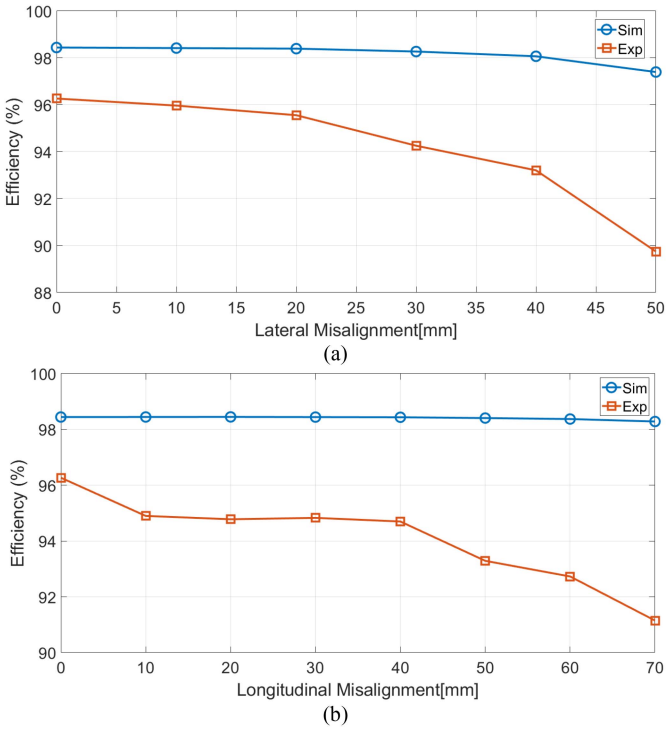

FIGURE 13. Efficiency versus (a) Lateral Misalignment (b) Longitudinal Misalignment.

as efficiency is determined by measuring the current and voltages at the out of the inverter and the input of the rectifier. The simulated plot does not include the losses in the ferrite core and the compensation capacitors. This is shown by the noticeable difference between the simulated and experimental plots. Losses in the compensation capacitors for lateral and longitudinal misalignment and change in load are illustrated in Tables 13 and 14. Losses in the primary side capacitors increase with misalignments due to the increase in primary current, while secondary losses almost remain constant as secondary current is constant due to the SS-compensated IPT system. A similar observation is valid for the variation of load resistance.

Both sets of analyses show a strong correlation between the simulated and experimental designs. In addition, Fig. 15 illustrates the variation of the transmitter and receiver inductance with respect to misalignment. Results show that both inductances remain stable during misalignment and will not result in the detuning of the IPT system.

Finally, a thermal analysis was done with the coils of C9. Fig. 16(a) shows the coils after five minutes of operation with a temperature reaching 27.7 °C. Fig. 16(b) shows the coils after ten minutes at which the system has reached a steady state. The results agree with the simulated analysis with C9 reaching a temperature of 30 °C at a steady state.

In summary, there is a close relation between simulated results and experimental results of C9, indicating that the design process was properly followed with no inconsistencies. Thus, the hardware prototype validates the effectiveness of the analysis provided in this study.

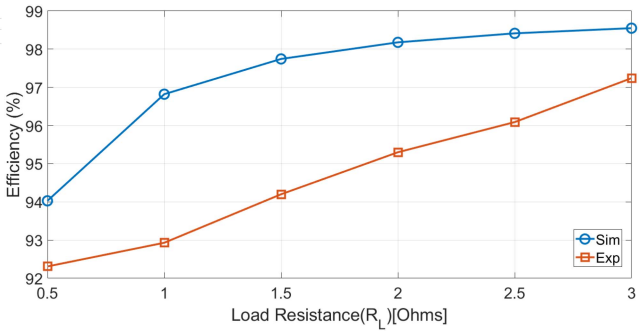

FIGURE 14. Efficiency versus Load Resistance.

TABLE 13. Compensation Capacitor Loss With Misalignment

Distance (mm)	$C_{1_{LAT}}(W)$	$C_{2_{LAT}}(W)$	$C_{1_{LONG}}(W)$	$C_{2_{LONG}}(W)$
0	3.53	5.26	3.53	5.26
10	3.54	5.26	3.65	5.26
20	3.8	5.33	3.86	5.3
30	4.26	5.33	4.12	5.36
40	5.57	5.4	4.48	5.38
50	8.02	5.47	5.06	5.39
60	NA	NA	6.14	5.43
70	NA	NA	7.61	5.48

NA: Not Applicable

TABLE 14. Compensation Capacitor Loss with Load Variation

$R_L(\Omega)$	$C_1(W)$	$C_2(W)$
0.5	1.41	5.17
1	1.72	5.16
1.5	2.15	5.2
2	2.71	5.26
2.5	3.48	5.18
3	4.31	5.21

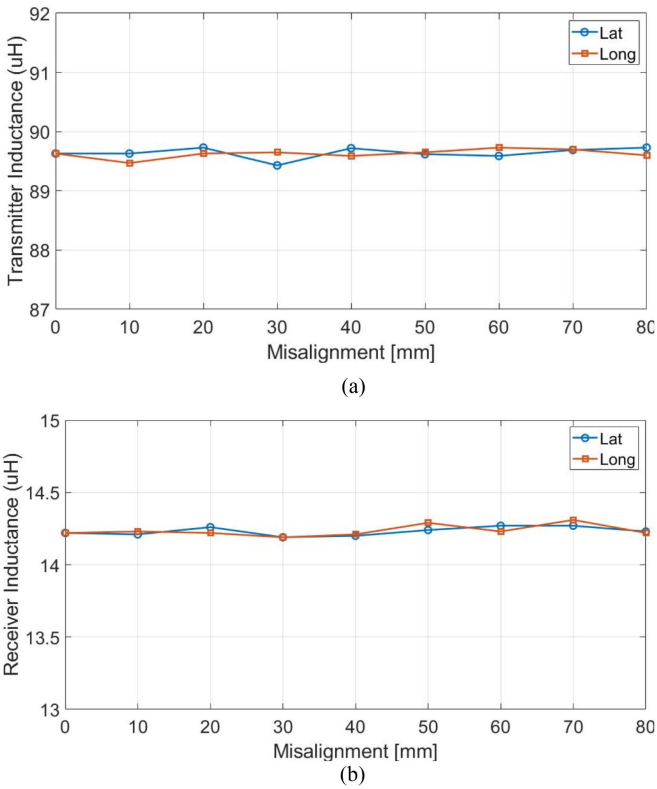

FIGURE 15. Change in inductance with misalignment (a) transmitter (b) receiver.

VI. DISCUSSION

The comparative analysis of magnetic couplers was conducted by evaluating the performance indices listed in Table 1. Design parameters and constraints listed in Table 3 formed the basis for the comparison so that couplers can be compared under similar conditions. SS compensation was used to model and match the couplers for the specified load (rated power). The properties of the couplers are shown in Table 4, and their overall performance is summarized in Table 10. Finally, the overall score is illustrated in Table 11.

It is evident that C1 performs best under all scenarios and is the superior coupler in terms of maximizing efficiency, minimizing weight, maximizing tolerance to misalignment, minimizing leakage field, and total harmonic distortion. It is followed by C6, the second best in maximizing efficiency and misalignment tolerance while minimizing weight and leakage field. However, it falls short of C8 in terms of minimizing THD. C7 is placed third in maximizing efficiency and misalignment tolerance while minimizing weight and leakage field. In summary, C1, C6, C7, and C8 are observed to have the best overall performance for existing UAV couplers.

The choice of compensation network is crucial in IPT applications. The analysis has shown that SS compensation can work for all couplers. However, this topology has some drawbacks for UAV applications. Since most IPT-based UAV applications have a light load, high coupling needs to be avoided to maintain an external quality factor (Q_e), which is greater than 3, and to meet the criteria for bifurcation-free operation. This means factors that affect the coupling coefficient, like transmission distance and mutual and self-inductances, must be considered properly before the design of coils. In addition, the choice of frequency is significant. Frequency in relation to the secondary inductance (L_2) affects the external quality factor (Q_e). Frequency in relation to mutual inductance (M) impacts the value of the primary current. It has been observed that a low mutual inductance can cause a high primary current. Therefore, the proper choice of frequency can compensate for this. Thus, transmission distance, frequency, and mutual and self-inductances are important considerations. Another observation made in the analysis was that the coil-to-coil efficiency reduces as the load resistance decreases and improves as the load resistance increases. This suggests that SS compensation is suited for high-power applications with

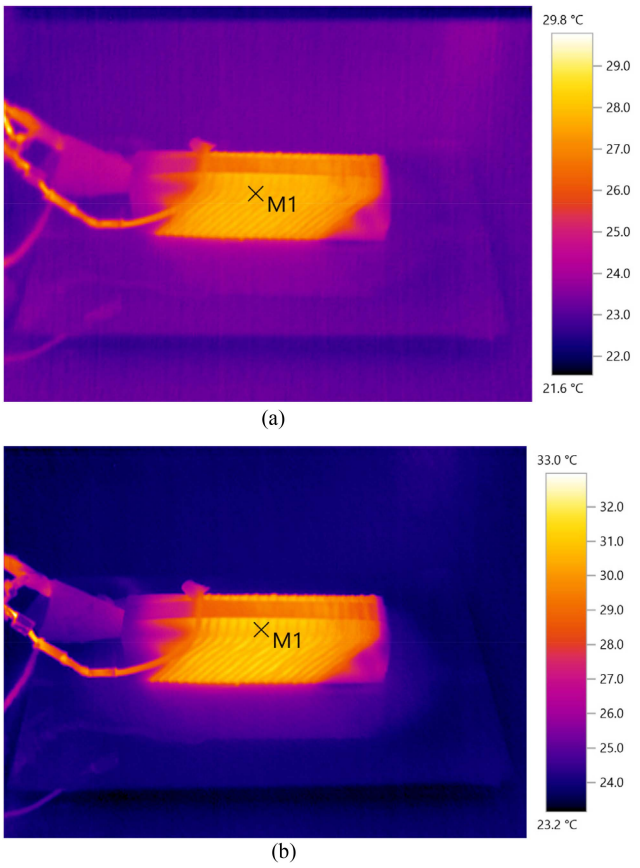

FIGURE 16. **Thermal Analysis of C9 (a) 5 min of operation (b) 10 min of operation.**

larger loads. Therefore, alternative compensation topologies should be investigated for UAV applications. The LCCL-S topology is highly efficient for low-power applications and less sensitive to load variations [25].

The loss analysis provided in Table 6 using (24)–(30) also shows that higher coil currents increase the total losses in the inverter and rectifier of an SS-compensated system. Primary coil current can be minimized by optimally designing the coupler parameters, such as mutual inductance, while the secondary coil current can be reduced by using an appropriate DC-DC converter to manipulate the load resistance [9].

Another contribution of this article in relation to existing literature is a thermal analysis of each coupler. The analysis was performed with ANSYS Icepak. The results show that a high power density is not the only factor contributing to high temperatures in the *Rx*-coil but is also impacted by the number of turns and the transmission distance between *Tx* and *Rx*-coils. An example of this is a comparison between C2 and C3. Both couplers have a similar number of turns on the *Rx*-coil and similar power densities. However, C3 has a shorter transmission distance between the *Tx* and *Rx*-coil and consequently shows a higher temperature. C9 is shown to have the highest temperature at steady state. The thermal loss in this coupler cannot be ignored as it contributes to the lower efficiency observed compared to other couplers in the analysis. Thus, a thermal analysis provides valuable information on the behaviour of couplers and should be considered in WPT applications.

VII. FUTURE DIRECTIONS

The following future directions are proposed based on the analysis performed in this article:

1. Most coils exhibit very high power densities. This is common in UAV applications due to smaller magnetic couplers, which can lead to higher-temperature coils. Optimization of couplers in terms of power density and thermal performance is critical for further improving the efficiency of these couplers.
2. In UAV applications, EMI and EMF exposure to humans is not a major threat, as most of the existing couplers studied in this article have shown that the magnetic field is safe beyond 30cm from the *Rx*-coil. The major challenge is to avoid the exposure of the field to sensitive electronics surrounding the IPT system. Minimizing EMI, using passive and active shielding, and implementing control for the power electronics are a few methods that can be studied further.
3. There is a lack of coil designs proposed for T-shaped and U-shaped legs. These are common landing gears in UAVs and should be given more attention in future studies.
4. Interoperability in couplers will be critical as different coils for different landing gears are proposed in the literature. Therefore, achieving a universal transmitter capable of charging different coils fitted to landing gears shown in Fig. 1 will revolutionize IPT-based UAV charging.

Investigation of alternative compensation topologies for IPT-based UAV applications should be considered. A comparative study using the LCCL-S can be implemented to observe the change in overall performance.

VIII. CONCLUSION

This article presented a comparative analysis between nine UAV couplers which have been proposed in the literature. Six significant performance indices were used as the criteria for comparison i.e., coil-to-coil efficiency, volumetric power density, leakage magnetic field, misalignment tolerance, weight of the *Rx*-coil and THD in the *Tx* and *Rx* currents. Detailed simulation analysis was performed with ANSYS Maxwell, ANSYS Icepak, and MATLAB Simulink. The design of each coil was carried out by following the design process identified in this article. An experimental prototype was conducted for one of the couplers to validate the efficacy of the comparative analysis. Results obtained from this article have identified the following:

1. Relative advantages and disadvantages of existing couplers under different scenarios where the importance of performance indices vary for each case.
2. Appropriate landing gears for each coupler.

3. Impact of compensation choice on coupler design.
4. Thermal behaviour of existing couplers.

In conclusion, the presented analysis provides a systematic comparison by considering all aspects of the IPT coupler in UAV applications. Furthermore, directions are provided for future work.

REFERENCES

[1] P. K. Chittoor, B. Chokkalingam, and L. Mihet-Popa, "A review on UAV Wireless charging: Fundamentals, applications, charging techniques and standards," *IEEE Access*, vol. 9, pp. 69235–69266, 2021.

[2] Y. Song, X. Sun, H. Wang, W. Dong, and Y. Ji, "Design of charging coil for unmanned aerial vehicle-enabled wireless power transfer," in *Proc. IEEE 8th Int. Conf. Power Energy Syst.*, 2018, pp. 268–272.

[3] C. Park et al., "Separated circular capacitive coupler for reducing cross-coupling capacitance in drone wireless power transfer system," *IEEE Trans. Microw. Theory Technol.*, vol. 68, no. 9, pp. 3978–3985, Sep. 2020.

[4] T. Campi, F. Dionisi, S. Cruciani, V. De Santis, M. Feliziani, and F. Maradei, "Magnetic field levels in drones equipped with wireless power transfer technology," in *Proc. Asia-Pacific Int. Symp. Electromagn. Compat.*, 2016, pp. 544–547.

[5] C. Cai, J. Wang, H. Nie, P. Zhang, Z. Lin, and Y.-G. Zhou, "Effective-configuration WPT systems for drones charging area extension featuring quasi-uniform magnetic coupling," *IEEE Trans. Transp. Electrific.*, vol. 6, no. 3, pp. 920–934, Sep. 2020.

[6] D. Ke, C. Liu, C. Jiang, and F. Zhao, "Design of an effective wireless air charging system for electric unmanned aerial vehicles," in *Proc. IEEE IECON- 43rd Annu. Conf. IEEE Ind. Electron. Soc.*, 2017, pp. 6949–6954.

[7] J. Zhou, B. Zhang, W. Xiao, D. Qiu, and Y. Chen, "Nonlinear parity-time-symmetric model for constant efficiency wireless power transfer: Application to a drone-in-flight wireless charging platform," *IEEE Trans. Ind. Electron.*, vol. 66, no. 5, pp. 4097–4107, May 2019.

[8] C. Song et al., "EMI reduction methods in wireless power transfer system for drone electrical charger using tightly coupled three-phase resonant magnetic field," *IEEE Trans. Ind. Electron.*, vol. 65, no. 9, pp. 6839–6849, Sep. 2018.

[9] C. Cai et al., "Development of a cross-type magnetic coupler for unmanned aerial vehicle IPT charging systems," *IEEE Access*, vol. 8, pp. 67974–67989, 2020.

[10] S. Obayashi, Y. Kanekiyo, K. Nishizawa, and H. Kusada, "85-kHz band 450-W inductive power transfer for unmanned aerial vehicle wireless charging Port," in *Proc. IEEE Wireless Power Transfer Conf.*, 2019, pp. 80–84.

[11] U. Gordhan and S. Jayalath, "A rectangular double-helix receiver coil for wireless charging of drones," in *Proc. IEEE Wireless Power Week*, 2022, pp. 361–365.

[12] T. Campi, S. Cruciani, and M. Feliziani, "Wireless Power Transfer Technology applied to an autonomous electric UAV with a small secondary coil," *Energies*, vol. 11, no. 2, 2018, Art. no. 352.

[13] A. Junaid, A. Konoiko, Y. Zweiri, M. Sahinkaya, and L. Seneviratne, "Autonomous wireless self-charging for multi-rotor unmanned aerial vehicles," *Energies*, vol. 10, no. 6, 2017, Art. no. 803.

[14] A. B. Junaid, Y. Lee, and Y. Kim, "Design and implementation of autonomous wireless charging station for rotary-wing UAVs," *Aerosp. Sci. Technol.*, vol. 54, pp. 253–266, 2016.

[15] A. Zaheer, H. Hao, G. A. Covic, and D. Kacprzak, "Investigation of multiple decoupled coil primary pad topologies in lumped IPT systems for interoperable electric vehicle charging," *IEEE Trans. Power Electron.*, vol. 30, no. 4, pp. 1937–1955, Apr. 2015.

[16] S. Choi, S. Huh, S. Lee, H. Kim, S. Woo, and S. Ahn, "Drone wireless charging station using multiple transmitter coils of different sizes with degrees of freedom in the Air Gap," in *Proc. IEEE 24th Int. Conf. Elect. Mach. Syst.*, 2021, pp. 722–726.

[17] S. Jayalath and A. Khan, "Design, challenges, and trends of inductive power transfer couplers for electric vehicles: A review," *IEEE J. Emerg. Sel. Topics Power Electron.*, vol. 9, no. 5, pp. 6196–6218, Oct. 2021.

[18] S. K. Bandyopadhyay, P. Venugopal, J. Dong, and P. Bauer, "Comparison of magnetic couplers for IPT-based EV charging using multi-objective optimization," *IEEE Trans. Veh. Technol*, vol. 68, no. 6, pp. 5416–5429, Jun. 2019, doi: 10.1109/tvt.2019.2909566.

[19] W. Zhang and C. C. Mi, "Compensation topologies of high-power wireless power transfer systems," *IEEE Trans. Veh.*, vol. 65, no. 6, pp. 4768–4778, Jun. 2016.

[20] V. Shevchenko, O. Husev, R. Strzelecki, B. Pakhaliuk, N. Poliakov, and N. Strzelecka, "Compensation topologies in IPT systems: Standards, requirements, classification, analysis, comparison and application," *IEEE Access*, vol. 7, pp. 120559–120580, 2019.

[21] H. Kim et al., "Coil design and measurements of automotive magnetic resonant wireless charging system for high-efficiency and low magnetic field leakage," *IEEE Trans. Microw. Theory Technol.*, vol. 64, no. 2, pp. 383–400, Feb. 2016.

[22] K. Aditya and S. S. Williamson, "Design guidelines to avoid bifurcation in a series–series compensated Inductive Power Transfer system," *IEEE Trans. Ind. Electron.*, vol. 66, no. 5, pp. 3973–3982, May 2019.

[23] P. Sun et al., "Analysis of frequency bifurcation and frequency splitting of IPT system under overcoupling," *Energy Rep.*, vol. 8, pp. 61–72, 2022.

[24] C.-S. Wang, G. A. Covic, and O. H. Stielau, "Power transfer capability and bifurcation phenomena of loosely coupled inductive Power Transfer Systems," *IEEE Trans. Ind. Electron.*, vol. 51, no. 1, pp. 148–157, Feb. 2004.

[25] Y. Chen, H. Zhang, S.-J. Park, and D. Kim, "A comparative study of S-S and LCCL-S compensation topologies in inductive power transfer systems for electric vehicles," *Energies*, vol. 12, no. 10, May 2019, Art. no. 1913, doi: 10.3390/en12101913.

[26] K. Woronowicz, A. Safaee, and T. R. Dickson, "Single-phase zero reactive power wireless power transfer topologies based on Boucherot Bridge circuit concept," *Can. J. Elec. Comput. Eng.*, vol. 38, no. 4, pp. 323–337, Fall 2015, doi: 10.1109/cjece.2015.2468057.

[27] Vishay Siliconix, "Zero-voltage switching full-bridge converter: Operation, FOM, and guidelines for MOSFET selection," vishay.com. Accessed: Jan. 16, 2024. [Online]. Available: https://www.vishay.com/docs/90936/an847.pdf

[28] Vishay Semiconductors, "How to calculate power losses in gen 5 diodes," vishay.com. Accessed: Jan. 16, 2024. [Online]. Available: https://www.vishay.com/docs/98280/howtocalculatepowerlossesingen5diodes.pdf

[29] A. Jahan, F. Mustapha, S. M. Sapuan, Y. Ismail, and M. Bahraminasab, "A framework for weighting of criteria in ranking stage of material selection process," *Int. J. Adv. Manuf. Technol.*, vol. 58, no. 1–4, pp. 411–420, May 2011.

UVIR GORDHAN (Student Member, IEEE) received the B.Sc. degree in mechatronics engineering in 2020 from the University of Cape Town, Cape Town, South Africa, where he is currently working toward the M.Sc. degree in electrical engineering. His research focuses on wireless power transfer.

SAMPATH JAYALATH (Member, IEEE) received the B.Eng. degree (Hons.) in electronic engineering from Sheffield Hallam University, Sheffield, U.K, in 2013, and the M.Sc. and Ph.D. degrees in electrical engineering from the University of Cape Town (UCT), Cape Town, South Africa, in 2016 and 2022, respectively. He is currently a Lecturer with the Department of Electrical Engineering, UCT. His research interests include filter design, control of power converters, wireless power transfer, and electromagnetic devices. He also chairs the IEEE IAS/IES/PELS combined South Africa chapter.